communications materials

A Nature Portfolio journal

Article

https://doi.org/10.1038/s43246-025-01011-x

Near-surface defects break symmetry in water adsorption on CeO_{2-x}(111)

Oscar Custance [1,7] ✉, Manuel González Lastre [2,7], Kyungmin Kim [3], Estefanía Fernández-Villanueva [2,4,5], Pablo Pou [2,6], Masayuki Abe [3], Hossein Sepehri-Amin [1], Shigeki Kawai [1], M. Verónica Ganduglia-Pirovano [4] & Ruben Perez [2,6] ✉

Water interactions with oxygen-deficient cerium dioxide (CeO_2) surfaces are central to hydrogen production and catalytic redox reactions, but the atomic-scale details of how defects influence adsorption and reactivity remain elusive. Here, we unveil how water adsorbs on partially reduced CeO_{2-x}(111) using atomic force microscopy (AFM) with chemically sensitive, oxygen-terminated probes, combined with first-principles calculations. Our AFM imaging reveals water molecules as sharp, asymmetric boomerang-like features radically departing from the symmetric triangular motifs previously attributed to molecular water. Strikingly, these features localize near subsurface defects. While the experiments are carried out at cryogenic temperatures, water was dosed at room temperature, capturing configurations relevant to initial adsorption events in catalytic processes. Density functional theory identifies Ce^{3+} sites adjacent to subsurface vacancies as the thermodynamically favored adsorption sites, where defect-induced symmetry breaking governs water orientation. Force spectroscopy and simulations further distinguish Ce^{3+} from Ce^{4+} centers through their unique interaction signatures. By resolving how subsurface defects control water adsorption at the atomic scale, this work demonstrates the power of chemically selective AFM for probing site-specific reactivity in oxide catalysts, laying the groundwork for direct investigations of complex systems such as single-atom catalysts, metal-support interfaces, and defect-engineered oxides.

Cerium dioxide (CeO_2, or ceria) is a cornerstone material in catalysis, widely used both as an active component and as a support, owing to its exceptional ability to store, release, and transport oxygen[1,2]. This redox flexibility is rooted in the ease of reversible Ce^{4+}/Ce^{3+} reduction, which enables ceria to form and heal oxygen vacancies under operating conditions. As a result, ceria exhibits remarkable versatility across a broad range of applications, from automobile exhaust gas treatment[3,4] and hydrogen production[5] to solid oxide fuel cells[6] and emerging biomedical technologies[7,8]. In common with other reducible oxides[9,10], the type, density, and spatial distribution of these vacancies profoundly influence catalytic performance. Among the molecular species central to redox catalysis, water plays a pivotal role, particularly in reactions such as the water-gas shift[11] and thermochemical splitting cycles[12]. Understanding how water interacts with defective ceria surfaces at the atomic scale is therefore essential for the rational design of next-generation catalysts and redox-active materials.

Atomic force microscopy (AFM) has proven to be a powerful tool to explore metal-oxide surfaces at the atomic scale, as well as adsorbates on them[13–17]. Constant-height imaging with functionalized probes[18–20] has empowered this technique with unprecedented resolution that has been deployed, among other feats, to study individual water molecules and properties of water networks on several surface systems[21–25].

Molecular water on ceria surfaces has been studied with AFM[26,27], as well as with scanning tunneling microscopy (STM)[28]. For both techniques, and for sample temperatures ranging from room temperature to 10 K, water molecules on the CeO_2(111) surface were imaged as wide triangular features extending over three surface oxygen atoms. At this surface, water adsorbs with the oxygen binding to a Ce^{4+} site and one of its hydrogen atoms interacting with one of the adjacent surface oxygen atoms[29]. In contrast to other oxides, water on CeO_2(111) can exist in two configurations, molecular form and hydroxyl pair[29–31]. This duality originates from the specific lateral

[1]National Institute for Materials Science (NIMS), Tsukuba, Ibaraki, Japan. [2]Departamento de Física Teórica de la Materia Condensada, Universidad Autónoma de Madrid, Madrid, Spain. [3]Graduate School of Engineering Science, Osaka University, Toyonaka, Osaka, Japan. [4]Instituto de Catálisis y Petroleoquímica (CSIC), Madrid, Spain. [5]Universitat Politècnica de València, Valencia, Spain. [6]Condensed Matter Physics Center (IFIMAC), Universidad Autónoma de Madrid, Madrid, Spain. [7]These authors contributed equally: Oscar Custance, Manuel González Lastre. ✉e-mail: custance.oscar@nims.go.jp; ruben.perez@uam.es

distance between the ceria site and its three neighboring oxygen atoms at the CeO_2(111) surface and the low energy cost of displacing these oxygen species. The low energy barriers between different adsorption configurations successfully explain the triangular shape detected in the experiments[29].

In this work, we study the adsorption of molecular water on a partially reduced CeO_{2-x}(111) surface using AFM operated at cryogenic temperatures (T ~ 4.8 K) with copper-oxide functionalized probes[19,20]. Our AFM images reveal water molecules as sharp asymmetric boomerang-like features, connecting the cerium adsorption site[29] with two of the neighboring surface oxygen atoms, challenging our understanding of water adsorption and imaging on the surface.

To clarify these new findings, we combine density functional theory (DFT) simulations with constant-height AFM imaging and site-specific frequency shift (Δf) curves[32,33] on both the surface atomic sites and the atomic positions visited by the water molecule. By comparing these Δf curves with theoretical predictions, we identified a model probe that reproduces the experiments well.

We build on this model to unveil the key role played by the response of the water molecule to the forces exerted by the probe during the experiments and explain the observed features in the AFM images, considering the presence of sub-surface oxygen vacancies. When such a defect is produced, two Ce^{4+} ions are reduced to Ce^{3+}. Our analysis suggests a particular adsorption environment created by one of these Ce^{3+} near a vacancy as the explanation for the asymmetry.

Furthermore, simulated Δf curves predict a stronger attractive interaction on the Ce^{3+} sites relative to the Ce^{4+}. This different interaction with the probe originates from distortions on the topmost oxygen layer caused by the excess charge localized on Ce^{3+}, and it paves the way for a possible experimental identification of these so far elusive defects.

Our work reveals the potential of AFM as a powerful atomic-resolution local technique to address and understand problems involving oxide nanostructures and their role in catalysis, such as the study of single-atom catalysts, due to the possibility of accessing the local reactivity.

Results and discussion

AFM imaging of water, surface atomic sites and probe identification

Figure 1a shows an atomic resolution AFM image of an area of the CeO_2(111) surface that presents four water molecules (see Fig. S1 for a general view of the surface region). Since it is well established that molecular water adsorbs on top of a cerium atom[27,29], these water molecules were used as markers[13] to assign chemical specificity to the atomic features observed in the AFM images and the Δf curves[32,33] measured over them (Fig. 1b, c).

The behavior of the experimental curves over the cerium and oxygen sites suggests an oxygen-terminated apex, which is consistent with the probe conditioning at the copper oxide areas[19] coexisting with the ceria islands (see the Methods). The nature of the probe apex is further confirmed by theoretical calculations of the Δf curves using a model probe that combines the short-range contribution from DFT calculated forces with the long-range probe-surface interaction (inset in Fig. 1d). The calculated forces are provided by a rigid CO molecule—that represents the oxygen atom at the apex—interacting with a stoichiometric CeO_2 slab (Fig. S9), which are then converted to Δf[34]. The long-range vdW interaction is obtained from a fitting to the experimental Δf curves at large distances (cyan dotted line in Fig. 1d, see also Fig. S9 and Methods). The calculated curves reproduce quantitatively the experimental spectroscopy, and allow us to estimate the value for the imaging distance ($Z_{exp} = 0$ in Fig. 1d), which corresponds to a Z ~ 411 pm separation with respect to the plane defined by the center of the uppermost surface oxygen atoms (Fig. 1d, see Methods). According to this distance and the Δf curves, the bright contrast in the constant-height AFM images relates to the topmost oxygen atoms of the surface, and the spots with the lower contrast correspond to the position of the cerium atoms below them (see the inset models in Fig. 1d).

A force curve on top of the water molecule informs us that the molecule is imaged in Fig. 1 past the minimum of the Δf curve; a region where the interaction between the probe and the surface has already become repulsive (see Fig. S2 for a detailed evolution of the AFM contrast over the water molecule with the distance). For surface atoms that correspond to the same chemical species, and with a similar charge state, the relative position of the Δf minima could be an indication of their topographic distribution normal to the surface. The minimum at a water molecule is 200 to 300 pm above the surface oxygen atoms, which is consistent with the results of our DFT calculations, where the oxygen atom of the molecule is 250 (220) pm above the cerium atom for the molecular (hydroxyl pair) adsorption state.

The images in Fig. 1 display two striking differences with respect to previous works[27,28,35]: (i), the triangular feature extending over three oxygen atoms is replaced by three well-defined lines connecting them; and (ii), one of the prongs of these lines presents a dimmer contrast than the other two, breaking the surface three-fold symmetry and giving rise to a boomerang-like shape (Fig. 1). This asymmetric shape is found in the three possible orientations compatible with the surface symmetry (see Figs. 1 and Fig. S2), and in all the cases, there is a dark shadow enclosed by two of the three lines, yet its location does not seem to correlate with the direction of the less intense one.

This asymmetric shape suggests either the stabilization of the dissociated state in the form of a hydroxyl pair, which naturally breaks the symmetry in one of the directions, or the presence of defects like oxygen vacancies and the associated Ce^{3+} ions nearby, that locally change the structure and energetics of water adsorption.

Water dosing in the experiments reported here was carried out at room temperature, resulting in a rather low coverage. Increasing the dosage by 10 and 100 times did not provide a significant increase in the concentration of water on our CeO_2(111) films. According to Mullins et al., water molecules do not adsorb on a fully oxidized CeO_2(111) surface at room temperature[36], suggesting that the adsorption of water on the CeO_2(111) surface at room temperature is significantly affected by the presence of defects. This would be consistent with our early works on the observation and manipulation of water molecules on CeO_2(111) single crystals with AFM[27,35]. Those crystals had a high density of defects (mostly subsurface defects characterized by contrast variations in topographic AFM images of the outermost oxygen surface layer, and occasionally, surface oxygen vacancies were also found), whose concentration and appearance varied from terrace to terrace[37]. The crystals had a black color, so they probably also contained atomic impurities. In those experiments, also carried out by similar dosing at room temperature, higher water coverage was obtained. Furthermore, while water was easily manipulated on the CeO_2(111) single crystals[35], our efforts to manipulate one of the water molecules displayed in Fig. 1a using a highly reproducible method we reported before[35,38] did not succeed (see Fig. S3).

Adsorption of molecular water in the presence of a subsurface defect

To understand the possible influence of defects in the adsorption of molecular water on the CeO_2(111) surface, we have performed first-principles calculations based on DFT as implemented in VASP[39–43] using the PBE[44] exchange-correlation functional supplemented with the vdW dispersion energy correction described by the DFT-D3 approach[45,46] (see Methods). There are DFT-based studies on the adsorption of water on CeO_2(111), (110) and (100) at low, intermediate and high coverages in the presence of surface oxygen vacancies[47–50]. However, we have previously demonstrated that the energetically most stable near-surface defect in the CeO_2(111) system is a subsurface oxygen vacancy (SSO_V)[51]. Accordingly, we have simulated the adsorption of a water molecule when an SSO_V is located nearby using a 3 × 3 unit cell.

In this 3 × 3 slab with one SSO_V, we have two equivalent Ce^{3+} sites and five inequivalent Ce^{4+} sites, of which two are nearest neighbors of the SSO_V (as in structure **3**, Fig. 2), whereas the others are farther away (as in structure **2**, Fig. 2; see also Fig. S5 and the associated discussion in the Supplementary Information). In the presence of a nearby SSO_V, the adsorption energy of the water molecule on a Ce^{4+} atom, −0.70 eV for the pristine surface[29–31] (Fig. 2a), is barely affected when the Ce^{4+} is a second neighbor to the

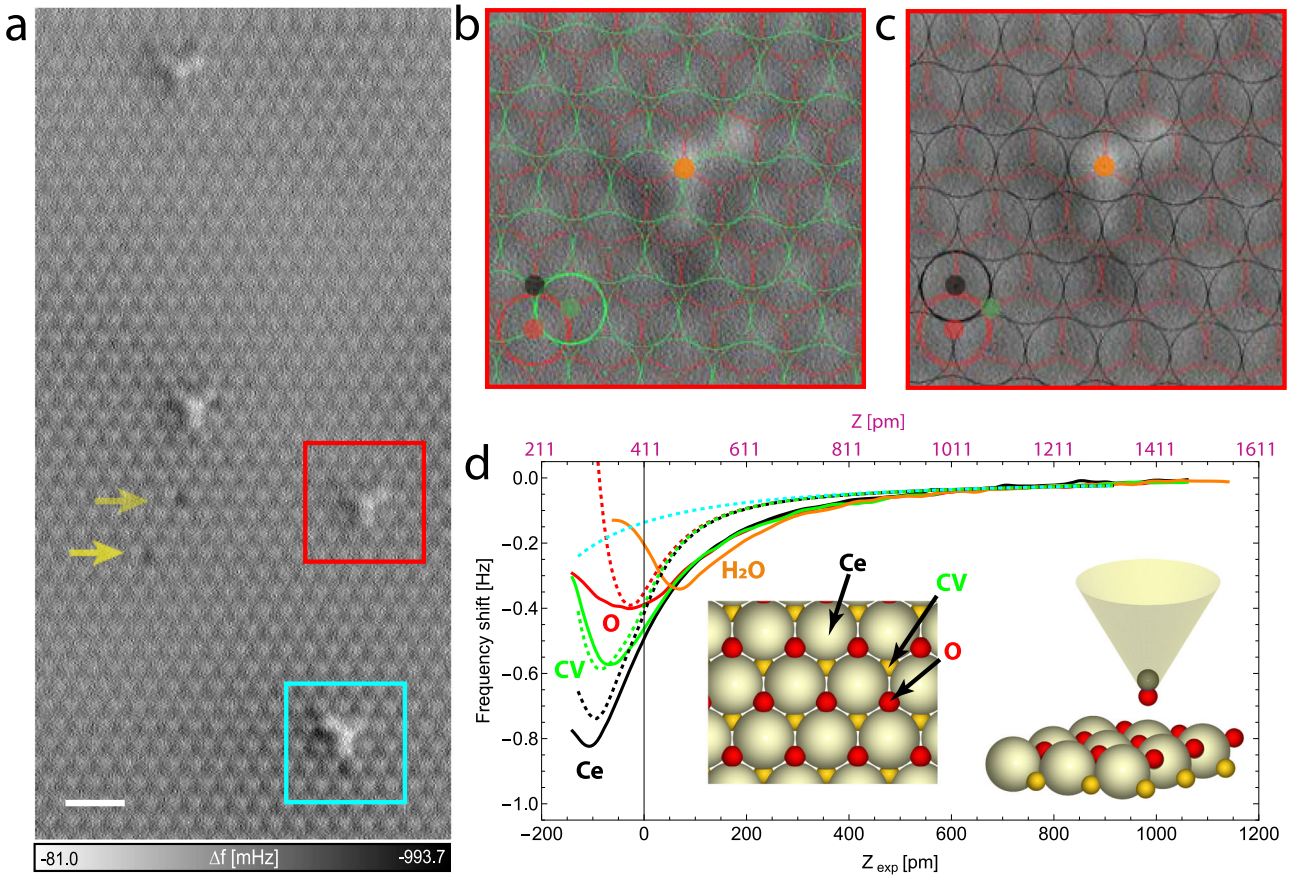

Fig. 1 | Individual water molecules, surface atom identification and probe-model characterization. a Atomic-resolution constant-height AFM image of a CeO_2(111) surface area displaying four water molecules, two of them enclosed by a red and a cyan square. **b**, **c** Water molecule highlighted with a red square in (**a**) with hexagonal lattices in red, green and black superimposed over the atomic sites of the CeO_2(111) surface: cerium (Ce), oxygen (O) and coordination vacancy (CV). The comparison of pairs of lattices with the adsorption position of the water molecule enables us to assign the black, red and green lattices to Ce, O and CV, respectively. **d** Frequency shift (Δf) curves measured at the top of the water molecule (orange), and on an O (red), a Ce (black) and a CV (green) site far from the molecule in (**b**, **c**). The dotted curves are calculated Δf curves from DFT interatomic forces obtained over the three CeO_2(111) surface sites using a probe modeled by a rigid CO molecule (inset). A long-range van der Waals interaction derived from fitting the experimental curves at large distances (cyan dotted line) has been added to each of the calculated curves to include the interaction with the mesoscopic part of the probe. The origin in the experimental distance axis (Z_{exp}) corresponds to the probe-surface separation the images in (**b**, **c**) were acquired. The correspondence $z_{exp} = 0 \Leftrightarrow z = 411$ pm has been determined by a rigid shift of all the simulated Δf curves in order to align their characteristic minima with those in the experiments. Acquisition parameters were: an oscillation amplitude (A) of 60 pm, and a free oscillation resonant frequency (f_0) of 994230 Hz. Yellow arrows in (**a**) point to Ce atoms with an unusual contrast. The scale bar represents 1 nm. See Methods for further details on AFM acquisition, model probe, calculated Δf curves, and fitting over the long-range interaction.

vacancy, -0.72 eV, but reduces (weaker binding) for first neighbors, with values in the range (−0.61, −0.66) eV (see Fig. 2b, Fig. S5). It is energetically more favorable for the water molecule to adsorb on a Ce^{3+} than on a Ce^{4+}, −0.79 eV (Fig. 2c). Under the presence of a SSO_V, the threefold symmetry observed for the pristine surface case[29] is broken, and an adsorption configuration with one of the hydrogen atoms interacting with a surface oxygen atom neighboring the SSO_V becomes the less favorable of the three possible molecular orientations, −0.68 eV vs −0.75 and −0.79 eV (Fig. 2c). When considering the hydroxyl pair, a lower adsorption energy is obtained over a Ce^{3+} than over a Ce^{4+} (−0.78 eV vs −0.75 eV, see Fig. 2d and Fig. S5), and attempting the formation of an hydroxyl with an oxygen neighboring the SSO_V results in recovering the molecular form (Fig. 2d). For the adsorption on a Ce^{3+}, the molecular and hydroxyl pair states are separated by energy barriers of ~ 50 − 60 meV (Fig. S6b); smaller than those found on a Ce^{4+} on the fully oxidized surface 80 (130) meV for the transition from (to) the molecular state (Fig. S6c). These calculations, carried out with the DFT-D3 approach to include the vdW interaction, compared well with our previous results[29] employing the optB86b-vdW functional, where binding energies of −0.73 (−0.76) eV were found for the molecular (hydroxyl pair) states, with energy barriers of 80 (100) meV for the transition from (to) the molecular state. Comparison with published theoretical results for water adsorption on a Ce^{3+}[52] shows that the inclusion of dispersion corrections provides an additional binding energy but does not significantly modify the relative stability of the different adsorption configurations for both the molecular state and the hydroxyl pair. Therefore, neither state is strongly thermodynamically favored, and both are expected to coexist at equilibrium.

This symmetry breaking and the energetic diversity among otherwise similar adsorption configurations for the water molecule close to the vacancy are due to the structural surface relaxations induced by the presence of the SSO_V and the two nearby Ce^{3+} ions[51]. Our calculations resulted in the oxygen atoms directly on top of the SSO_V relaxing ~15 pm towards the bulk. In contrast, the second nearest surface oxygen atoms and the Ce^{3+} rise ~ 15 pm and ~ 7 pm, respectively, toward the vacuum (Fig. 6d, e). We have carefully checked that all of these conclusions are not conditioned by the particular arrangement of the Ce^{3+} ions forced by the 3 × 3 cell (where they are neighbors), as shown by the results for adsorption structures (Fig. S7) and energy barriers (Fig. S8) obtained in a 4 × 4 unit cell (see Methods).

Calculated AFM images of a water molecule adsorbed near a subsurface defect

To explore whether the presence of the SSO_V and associated Ce^{3+} ions explain the asymmetric shape found in our experiments, we calculated

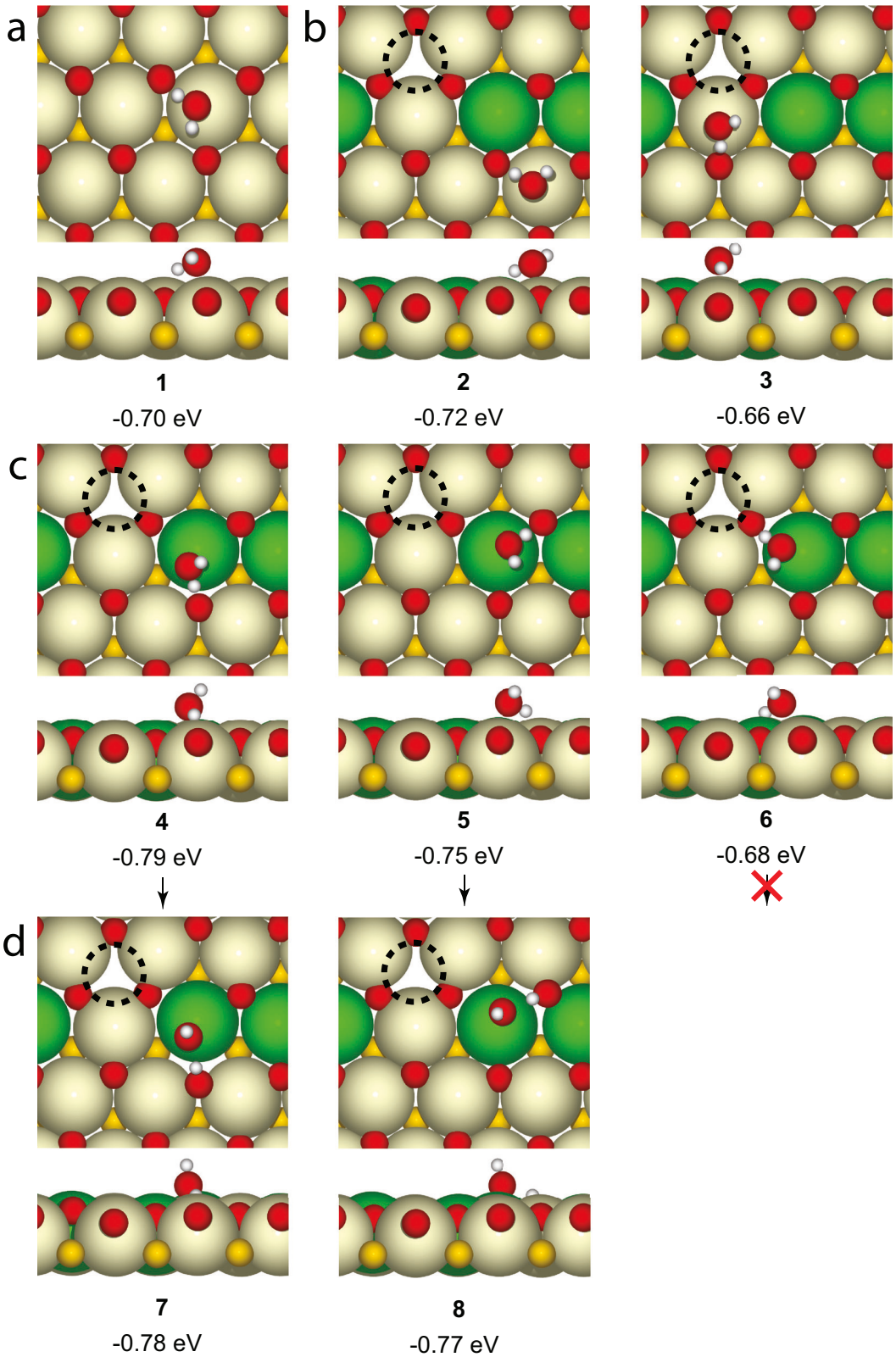

Fig. 2 | Water adsorption at the CeO_2(111) surface in the presence of a subsurface oxygen vacancy. DFT optimized most stable structures for water adsorption on: **a** a Ce^{4+} of the pristine surface; **b** a Ce^{4+} of the reduced surface, far **2** and close **3** to the oxygen vacancy; and **c** a Ce^{3+} of the reduced surface. **d** Hydroxyl pair (OH + H) adsorbed on a Ce^{3+} and a neighboring O atom of the reduced surface. The energies with respect to the slab and water molecule energy are indicated. The position of the oxygen vacancy is highlighted by a dotted circle. Ce^{3+}, Ce^{4+} and surface O and subsurface O atoms are represented in green, beige, red and yellow, respectively. No stable hydroxyl pair (OH + H) was obtained from structure **6**; it reverts to water.

constant-height AFM images at several probe-surface separations using representative stable configurations for the adsorption of water close to a SSO_V (Fig. 3). These calculations are based on the full density–based model (FDBM)[53,54]—which retains DFT accuracy in the description of the probe-surface forces while offering the computational speed needed for simulating a whole image—using the probe model shown in Fig. 1. Therefore, the calculated Δf signal for these images includes both the short-range contribution from the CO molecule (calculated with FDBM) and the long-range vdW interaction fitted from the experiments.

In a constant height AFM image, the contrast will depend on the relative value of the probe-surface forces over the different surface positions explored. In the images presented in this work, the dark regions (normally more negative Δf) correspond to a stronger net attraction between the probe and the surface, whereas brighter areas reflect a less attractive interaction, because either the force is small or it already ascends the repulsive branch of the interaction, in a manifestation of the non-monotonic nature of the probe-surface interaction force. An example of this effect appears in the contrast of the AFM images in Fig. 1: while the contrast over the surface oxygen atoms and over the water molecule seems to be similar, the former corresponds to an attractive interaction and the latter to the onset of a repulsive one. In the calculated images in Fig. 3, the subsurface Ce positions appear as a relatively bright background even though the interaction between the terminal oxygen of the probe and the Ce site remains attractive (Fig. 1d). This apparent brightness arises because the strong attractive contribution from the hydrogen bond between the water molecule and the probe that saturates the color scale used for the maps.

Figures 3a, b present calculated Δf images of the two most stable configurations for the water adsorption on a Ce^{3+} atom in the molecular form (**4** and **5** in Fig. 2, respectively). These orientations show a bright contrast over a region close to the oxygen of the molecule, and display an extended dark feature over a wide area spanning from the position of the hydrogen atom pointing upwards towards the surface oxygen atoms opposite to the SSO_V.

The probe-surface separations explored (540–500 pm) covers the regime where the bright contrast over the oxygen atom of the molecule starts to be dominated by the Pauli repulsive interaction between the lone pairs of the oxygen atoms of CO and water; consistent with the appearance of a bright contrast—of repulsive nature, as it develops past the Δf minimum—at the water site in Fig. S2. The dark contrast reflects the attractive interaction associated with the onset of a hydrogen bond formation between the hydrogen pointing upwards and the oxygen atom at the CO molecule, which is consistent with the vertical electric field resulting from the DFT simulations (Fig. S19). For an analysis of the force contributions for the representative case of Fig. 3a, see Fig. S10.

In the hydroxyl pair case (configuration **7** in Fig. 2d), the imaging mechanism is similar (Fig. 3c): an initial dark contrast is obtained due to an attractive interaction of the hydrogen atom pointing towards the vacuum with the oxygen atom at the probe, that develops into a bright spot upon further approach towards the surface, as the repulsive interaction between the oxygen of the hydroxyl and the one at the probe starts dominating the contrast (see Fig. S11 for the corresponding force contributions).

These calculated Δf images point towards the AFM being capable of discriminating between the two adsorption forms upon stabilization of one of them on the surface. However, the calculated images only partially reproduce the observed features in the experiments. The calculated AFM images were obtained under the common assumption that the surface configuration is not modified by the interaction with the probe. Yet our DFT calculations suggest that water is extremely mobile in either of the two forms on $CeO_2(111)$[29]. Further information about how the water molecule interacts with the probe can be obtained from the calculation of Δf curves over the relevant atomic positions visited by the molecule.

Interaction of the probe with the water molecules

Figure 4 displays calculated Δf curves over the atomic sites of a fully oxidized $CeO_2(111)$ surface in the presence of a water molecule. In the calculation of the forces that generate these curves (Fig. S12), the outermost oxygen-cerium-oxygen trilayer of the surface and the water species were allowed to

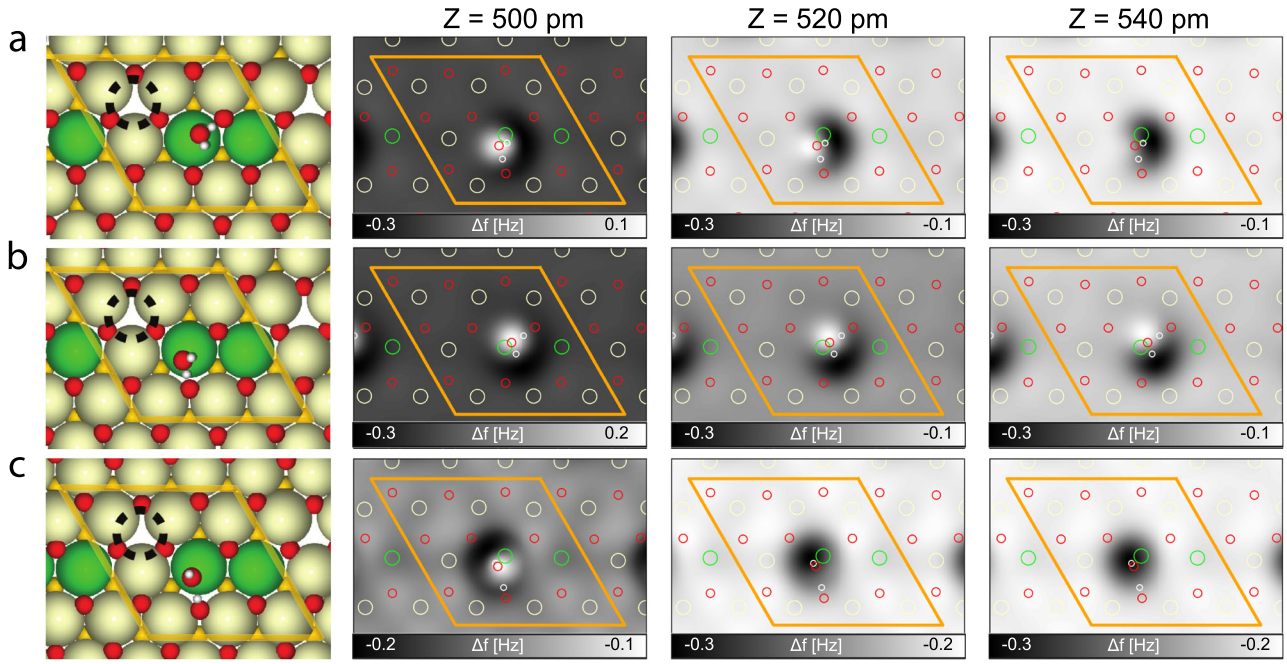

Fig. 3 | Simulated constant-height AFM images. Calculated Δf maps of the most stable adsorption configurations of a water molecule adsorbed on a partially reduced $CeO_{2-x}(111)$ surface characterized by the presence of a subsurface oxygen vacancy (dotted circumference). The Δf images were calculated using the full density based model (including the probe-surface long-range vdW interaction fitted from the experiments, see Methods) at three representative probe-surface separations for: **a** molecular water in configuration **4**; **b** molecular water in configuration **5**; and **c**, hydroxyl pair in configuration **7**, as shown in Fig. 2. Latices with the top-most Ce and O surface atomic positions, as well as a rhomboid highlighting the unit cell, have been superimposed to each Δf image. The color code for the species in the atomic models is the same as for Fig. 2. See Figs. S18 and S19 for the corresponding charge density and vertical electric field maps, respectively.

relax in response to the force exerted by the probe model introduced in Fig. 1. Each set of Δf curves comprises the interaction over the cerium site the water binds to (orange), the three neighboring surface oxygen atoms (yellow, cyan and magenta), and an oxygen atom of the fully oxidized surface (red) for reference.

The calculated Δf curves for the adsorption of water in molecular form (Fig. 4a) reveal a strong variability in the magnitude and position of the minima over the oxygen atoms. The water molecule pulls the oxygen involved in the hydrogen bond up by ~ 10 pm with respect to the other two oxygen atoms, whose heights are unaffected by the presence of the molecule. This structural modification is amplified by the water-probe interaction, causing the corresponding Δf minimum to be shifted by ~100 pm towards the vacuum (yellow curve) with respect to the reference surface oxygen. The proximity of the water molecule also affects the position and magnitude of the Δf minimum for the oxygen atom labeled in magenta, while the Δf curve over the oxygen far from the hydrogen atom (cyan) is the closest to the reference oxygen.

A dominant role of the interaction over structural effects manifests in the curve at the cerium site: although the oxygen of the water molecule is ~ 170 pm higher than the yellow-labeled oxygen, the attractive interaction provided by the hydrogen atom pointing out of the surface reduces the difference in the position of the curve minimum to ~ 75 pm. Despite that this hydrogen has a lower height than in the case of the adsorption on a Ce^{3+}, the contrast evolution over the cerium site at large distances is consistent with the one shown by the images calculated with FDBM for the reduced surface, with the orange curve bending upward and crossing those associated with the neighboring oxygen atoms for distances below 540 pm.

The hydroxyl pair provides smaller differences among the three oxygen sites, and shows greater flexibility of the atoms to move in response to the interaction with the probe, which changes the position and strength of the Δf minima for the cerium site and the yellow-labeled oxygen with respect to the molecular adsorption case.

Our experiments also reveal an asymmetric behavior of the Δf curves over the atomic sites visited by the water molecule. Figure 5a displays the curves obtained at the location highlighted by a red square in Fig. 1a; and Fig. 5b, c shows two sets of curves measured over the molecule enclosed by a cyan square in Fig. 1a, but with a 40-minute interval between their acquisition.

A close look at the contrast of the atomic sites in the image displayed in Fig. 5a reveals a discrepancy with the spectroscopic data. Two of the oxygen atoms (cyan and magenta) show a bright contrast, while the third one (yellow) has the appearance of a normal surface oxygen atom. The associated Δf curves indicate, however, that the contrast over the spots in yellow and magenta should be almost identical to the contrast on a standard surface oxygen. The sets displayed in Fig. 5b, c show similar discrepancies: in Fig. 5b, the spot in yellow should have a dimmer contrast than the one in cyan; and in Fig. 5c, the sites highlighted in yellow and cyan should have almost identical contrast, but in the image, the cyan spot appears dimmer than the yellow one. This discrepancy between the image contrast and the corresponding Δf curves, together with the variability of the Δf curves recorded at different times over the same molecule, points to the existence of probe-induced dynamical effects that result in the change of the adsorption configuration of the water molecule, and possibly, reversible transitions between molecular and hydroxyl pair forms.

Probe-induced dynamical effects

These probe-induced changes have been verified during the simulations to produce the calculated Δf curves. In Fig. 4a, an abrupt instability upon approaching the probe beyond 420 pm over the yellow-labeled oxygen atom brings the Δf curve very close to the one at the magenta site, generating what seems to be a minimum. However, this sharp feature reflects in reality a transition between force spectroscopy curves that correspond to two different configurations of the system. This formation originates from a probe-induced change in the adsorption configuration, in which the hydrogen atom interacting with the oxygen at the yellow site moves upward, breaks the hydrogen bond, and then the whole molecule rotates to establish a new hydrogen bond with the oxygen atom at the magenta site (see Movie S1). In this new arrangement, the yellow site plays an equivalent role to the magenta site in the original configuration, explaining the similarity between the two Δf curves beyond 400 pm approach. Similar processes take place when the probe approaches other sites, like the coordination vacancy between the oxygen atoms marked in yellow and cyan (see Movie S2), confirming that this event—characterized by a very low energy barrier[29]—is quite common for the probe-surface separations used in atomic resolution imaging (~ 411 pm for the images in Fig. 5). Interestingly, the probe is also able to induce the transition from the molecular form to the hydroxyl pair when approaching over the cerium site (see Movie S3). In this case, the proton transfer occurs spontaneously—indicating a zero energy barrier—in the range of 385–400 pm, close to the imaging separation mentioned above. This transition will seamlessly switch between the orange curves in Fig. 4a, b, bringing the position of the minimum—relative to the ones for the oxygen sites—and its strength closer to the experiment. Within the accuracy of our calculations, the molecular and hydroxyl-pair states adsorbed on a cerium atom (either a Ce^{3+} or a Ce^{4+}) have nearly the same energies, which differ only on a few tens of meV (Fig. 2), and the activation barriers for interconversion are likewise small (Fig. S6). Therefore, the two states are thermodynamically comparable and expected to coexist, with switching readily triggered by the probe under our imaging conditions at 4.8 K. In the experiments, the separation at which this transition occurs is well beyond the minimum in the calculated Δf curves, entering a probe-surface interaction range dominated by the repulsion between the oxygen atoms of the molecule and the probe. The limitation of our model to describe areas of highly repulsive forces, where the long-range elasticity of probe and surface starts playing a role, makes the theoretical curves significantly steeper than the experimental ones past the minimum of the Δf. However, considering that the water molecule is imaged in the experiments under this repulsive interaction regime, our calculations strongly suggest that the transition between molecular form and hydroxyl pairs should take place systematically during imaging.

With all this information, we can address the appearance of the molecule as three well-defined lines pointing to the neighboring oxygen atoms with a boomerang-like shape.

Origin of the boomerang-like shape of water in the AFM images

When imaging with CO-functionalized probes, the relaxation of the CO molecule in response to the interaction with the surface enhances the AFM signal over covalent[18,55] and hydrogen[53,55] bonds, which are imaged as bond-like sharp features. In our experiments and simulations, we use a rigid oxygen-terminated apex, yet the probe-induced transitions of the water molecule between the different adsorption configurations play a similar role to the relaxation of the CO molecule, leading to the three well-defined lines observed in our experimental images. These transitions are not privative of the molecular form: Movie S4 shows a probe-induced change in the orientation of the hydroxyl pair that closely resembles the dynamics of a flexible CO-apex in the presence of a rapidly varying region of the potential energy surface.

These probe-induced relaxations would tend to restore the threefold symmetry. However, the discussion above shows that both the presence of defects such as a SSO_V and the water molecule itself—that pulls up a surface oxygen atom with the hydrogen bond—contribute to break the symmetry among the three neighboring oxygen sites. A quantitative answer to this question would imply DFT simulations of force curves for a water molecule adsorbed on different cerium sites on a reduced ceria surface on a fine 3D grid of the probe positions. The inclusion of just a single SSO_V with the two associated Ce^{3+} ions in those calculations renders the relaxation of the whole system to the ground state for each probe position a herculean feat, as the Ce^{3+} ions make the electronic convergence quite cumbersome. Such calculation is beyond our current capabilities, but we can point out that the presence of an SSO_V singles out the oxygen site closer to the vacancy, making less probable the formation of a hydrogen bond with that site in the countless times the water molecule visits the three oxygen atoms during an AFM image.

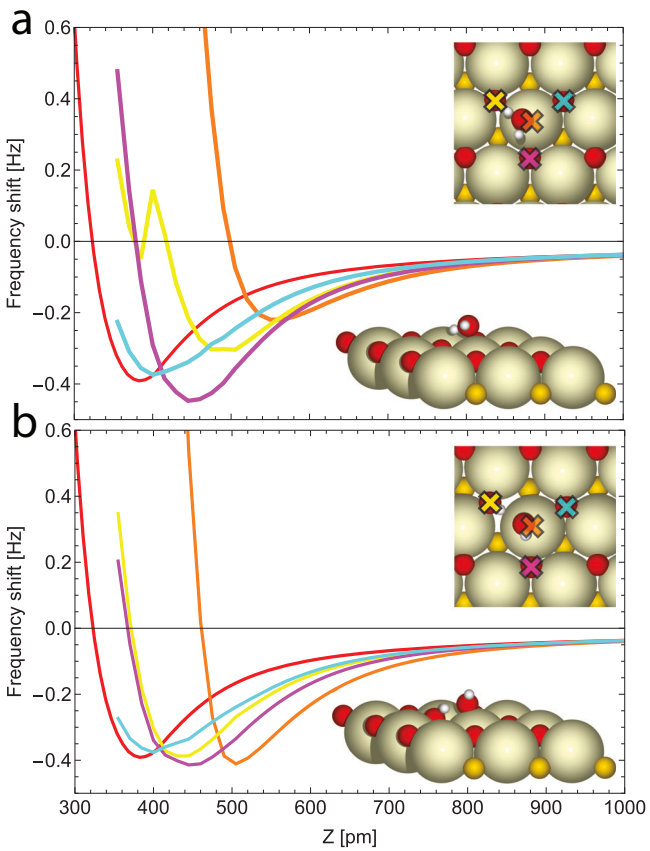

Fig. 4 | Calculated spectroscopy curves for a water molecule on a fully oxidized CeO_2(111) surface. Sets of calculated Δf curves over the surface atoms visited by a water molecule adsorbed on the CeO_2(111) surface: the Ce atom the molecule binds to (in orange) and its three first-neighboring oxygen atoms (in yellow, cyan and magenta). **a** Water in a molecular form; and **b** water in hydroxyl pair form. The inset images are top and side views of the atomic conformations of the molecule and surface atoms. The Δf curve over a surface O atom in the absence of the water molecule (curve in red, Fig. 1d) has been included for reference. The calculation of the Δf curve over the center of each surface atom (colored crosses) was performed to match the experimental counterparts (see Fig. 5). The probe model introduced in Fig. 1, including the probe-surface long-range vdW interaction fitted from the experiments, was used for the calculation of the Δf curves (see Methods).

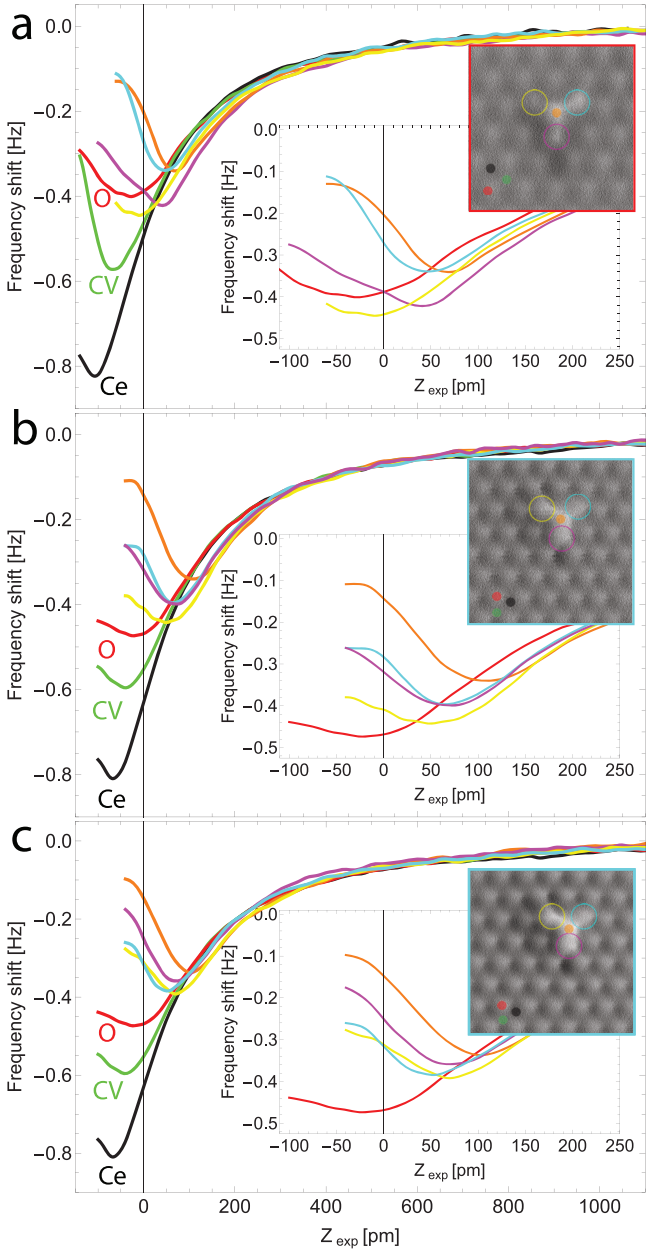

Fig. 5 | Spectroscopic measurements over water molecules. Frequency shift (Δf) curves obtained over the center of the water molecule structure (orange) and the center of the three surface oxygen atoms (yellow, cyan and magenta) the molecule visits. The inset graphs show a detail around the minima of the Δf curves. These sets of force curves were measured over: **a** the molecule highlighted with a red square in Fig. 1a; **b** the molecule highlighted with a cyan square in Fig. 1a; **c** the same molecule as in **b**, but 40 minutes after the acquisition of the first set. Constant-height AFM images obtained prior to the force spectroscopy measurements are included as insets. Each image was measured at a probe-surface separation corresponding to the origin of the distance axis. A set of force curves over the three surface sites of the CeO_2(111) surface (Ce in black, O in red, and CV in green) far from the water molecule is included for reference. All curves were measured with an identical probe apex termination. Acquisition parameters were: A = 60 pm and f_0 = 994230 Hz.

In the experiments reported here, direct evidence of the presence of subsurface oxygen vacancies could not be obtained either in the Δf or in the dissipation signal; the latter is probably due to the use of a much stiffer force sensor[56,57] than in previous works[37]. However, we often observe cerium atoms with an unusual contrast (yellow arrows in Fig. 1a) in a concentration close to the coverage of water molecules on the terraces after dosing water at room temperature. We propose that these more attractive cerium atoms can be candidates for Ce^{3+}, originating from the presence of defects under the surface.

Origin of the cerium atoms with unusual contrast

To address the nature of these cerium atoms, we calculated Δf curves on different cerium sites of the reduced surface (Fig. 6a) using the model probe introduced in Fig. 1. In order to speed up the calculation of the forces, and to single out the effect of the presence of the vacancy, we have not included the water molecule in these DFT simulations.

Our calculations reveal that the Ce^{3+} sites have the deepest Δf minimum (18% larger than the Ce^{4+} labeled 1, and 9% larger than the reference Ce^{4+} on the fully oxidized surface), which is associated with a significantly stronger attractive force with the probe compared to the Ce^{4+} sites (see Fig. S13).

This outcome seems counterintuitive when considering the extra screening provided by the additional electron localized at the Ce^{3+} site. However, an increase in the local electric field over the Ce^{3+} as a result of surface atomic relaxations accounts for this stronger interaction. Figure 6b, c show the vertical component of the local electric field (E_z) for the fully oxidized and the reduced ceria surface,

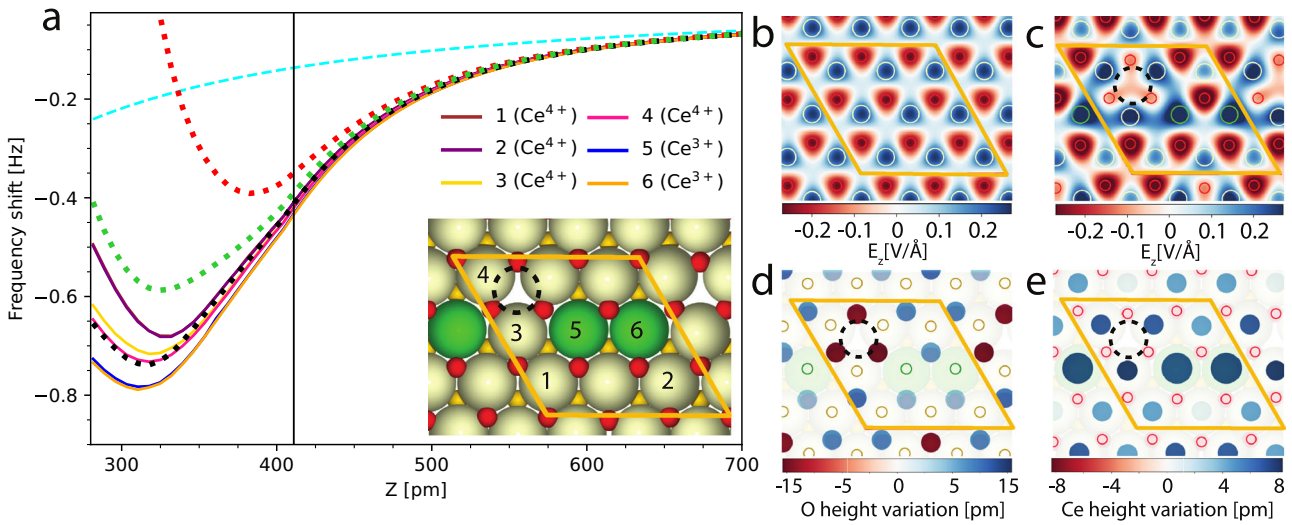

Fig. 6 | Calculated frequency shift curves over cerium atoms in the presence of a vacancy. a DFT-based calculated Δf over the Ce^{4+} (curves 1–4) and the Ce^{3+} (curves 5 and 6) atoms of a reduced $CeO_{2-x}(111)$ surface in the vicinity of a subsurface oxygen vacancy (dotted-line circles). Curve labeling is indicated in the inset image displaying the atomic arrangement, which also serves as a reference for the atomic features presented in the other panels. The Δf curves for the O (red), Ce (black), CV (green) calculated for the fully oxidized surface (Fig. 1), together with the long-range vdW component (cyan) fitted from the experiments, have been included as dotted lines for reference. This long-range vdW contribution has also been added to the calculated Δf curves in the graph. **b**, **c** Local distribution of the vertical component of the electric field (E_z) for the fully oxidized surface and for the same area with a subsurface oxygen vacancy (dotted circle), respectively, both obtained at a height of 274 pm above the topmost oxygen layer. **d** Vertical relaxation of the surface oxygen atoms near a subsurface oxygen vacancy with respect to the position of the topmost oxygen layer of the fully oxidized surface. **e** Vertical relaxation of the cerium atoms in the proximity of a subsurface oxygen vacancy with respect to the position of the outermost cerium layer of the fully oxidized surface (78 pm below the uppermost oxygen layer). The parallelogram in orange highlights the unit cell used in the calculations.

respectively, at a height of 274 pm above the uppermost oxygen layer. The strong E_z over the Ce^{3+} sites comes from the displacement of the nearby oxygen atoms away from the Ce^{3+} (see Fig. S14) due to the excess charge localized in the Ce^{3+} as a polaron, enhancing the attractive short-range electrostatic interaction and reducing the Pauli repulsion sensed by the AFM probe. The downward displacement of the oxygen atoms around the SSO_V (Fig. 6d) and the slight upward shift of the Ce^{4+} sites close to it (Fig. 6e) also contribute to the enhanced E_z. These simulations set the basis for the possibility of identifying the presence and location of the elusive Ce^{3+} ions using spectroscopy measurements, supporting our interpretation for the cerium atoms with an unusual contrast found in the terraces[58].

We observed similar variability in the interaction with the cerium atoms in the vicinity of the water molecules. Figure 7 summarizes Δf curves measured over atomic positions around the molecule highlighted with a red square in Fig. 1a (see also Fig. S4). The cerium atoms at the vertices of the triangle formed by the water structure (curves 1, 2, 3 in cyan) show ~ 9% and ~ 6% greater minimum value than the reference cerium far from the molecule (black curve). The three cerium sites on the left (curves in orange) show similar response as the reference atom, but the three cerium sites on the right (curves 7, 8, 9 in blue), which should be equivalent by symmetry, show a more repulsive interaction past the minimum. Similar strong repulsion is also detected over the second line of surface oxygen atoms on the right (positions and curves in pink). The water molecule visiting more often the oxygen atoms on the right and lower sides than the left one undoubtedly plays a role in adding steepness to the Δf curves beyond the minima over the cerium atoms in blue, the oxygen sites in pink and, to a lesser degree, the cerium at position 4. However, the cerium atoms at positions 1, 2, 3 (in cyan) are far enough to be affected by the water molecule, and the consistency with the theoretical calculations points them out as candidates to Ce^{3+} ions, suggesting the possible presence of SSO_V close to the adsorbed water molecule.

At this point, we cannot rule out the presence of a SSO_V close to the cerium atoms with an unusual strong attractive interaction in both the middle of the terraces and around the water molecules, but we speculate, considering the difficulty in increasing the water coverage on the surface when dosing at room temperature, that the presence of one or several SSO_V close to the Ce^{3+} ions is needed to bind water molecules to the terraces of the $CeO_2(111)$ surface at room temperature. Addressing this and other questions will require future work, exploiting the sensitivity of AFM spectroscopy in combination with tunneling measurements[51] that could help locate the SSO_Vs.

Conclusions

In summary, we have combined Non-Contact AFM and first–principles calculations to investigate the interaction of water with a partially reduced $CeO_{2-x}(111)$ surface at the atomic scale. Our low-temperature experiments using oxygen–terminated probes reveal water molecules adsorbed on cerium atoms as sharp, asymmetric boomerang–like features, in contrast with previous STM and AFM studies, in which water appeared as a triangular shape, consistent with the symmetry of the lattice surface. DFT simulations reveal that water—in both molecular and dissociated forms—preferentially adsorbs at Ce^{3+} sites near subsurface oxygen vacancies, and the surface relaxations induced by these defects break the local symmetry of the lattice. Calculated force spectroscopy based on DFT exhibits distinct interaction signatures between the Ce^{3+} and Ce^{4+} sites. These differences are attributed to local structural relaxations of surface oxygen atoms, which change the local electrostatic environment of the cerium species. These calculations match quantitatively with experimental force spectroscopy measurements around the water molecule and on the reduced surface. Finally, the characteristic contrast in constant-height AFM images originates from a probe-induced mobility of the water molecule, enabled by low-energy barriers between different adsorption configurations and adsorption states, and possibly, from the particular environment created around a Ce^{3+} ion close to a subsurface oxygen vacancy. Beyond resolving water adsorption on the $CeO_2(111)$ surface, our work demonstrates the broader capabilities of chemically selective AFM for probing local chemical reactivity. This approach offers a unique opportunity to investigate, at the atomic level, complex catalytic systems including single-atom catalysts, metal-support interfaces and defect-engineered oxide surfaces, where local structure and charge state critically influence chemical behavior.

Methods

Scanning probe microscopy experiments

The experiments were carried out in an ultra-high vacuum (UHV) system equipped with tools for the in situ sample preparation and a home-made scanning probe microscope operated at 4.8 K using a commercial controller (Nanonis SPM Control System, SPECS, Germany). AFM experiments were carried out using the frequency modulation detection scheme[59] keeping constant the oscillation amplitude of the force sensor. Under this scheme, the AFM signal corresponds to the shift in the free-oscillation resonant frequency of the force sensor (Δf) upon forces acting on it. Force spectroscopy experiments were performed by initially approaching the probe towards the surface from the imaging separation, and then retracting it upon reaching the specified closest approach until reaching the free-oscillation regime. Both constant-height AFM imaging and spectroscopy were carried out by setting the voltage bias to zero. CeO_2(111) thin-films were grown on a Cu(111) surface following a similar procedure to the one described elsewhere[60]. The Cu(111) single crystal was cleaned by repeated cycles of argon ion sputtering and annealing in UHV, and then the surface was oxidized by keeping the sample at 470 °C in a 1.0×10^{-5} Pa oxygen environment for 10 min. The CeO_2(111) thin-films were fabricated by depositing cerium (rod, 99.9 % purity, GoodFellow) from a water-cooled e-beam evaporator in the presence of 1.0×10^{-5} Pa oxygen while keeping the pre-oxidized Cu(111) sample at 480 °C. After the cerium evaporation, the sample temperature was gradually reduced at a typical rate of 1°C/sec in an 1.0×10^{-5} Pa oxygen. Upon the sample reaching 200 °C, both heating and oxygen flow were stopped and the crystal was left to cool to room temperature in UHV. Ultra-clean Milli-Q water, further purified by several freeze-pump-thaw cycles, was dosed by backfilling the UHV preparation chamber with water vapor through a leak valve while keeping the sample at 35 °C. Dosing with 5, 50 and 500 Langmuir of water with the sample at 35 °C produced similar coverages as the one displayed in Fig. 1.

Probe preparation

We used the KolibriSensor (SPECS, Germany) for the detection of both tunneling current and probe-surface interaction forces. The probe of the KolibriSensor was sharpened to a typical apex radius of ~ 15 nm ex situ by using a focused ion beam, and it was further conditioned for atomic resolution imaging in situ on copper oxide surface areas coexisting with the CeO_2(111) thin-films. Probe conditioning is carried out until good and sharp atomic resolution is obtained, and force spectroscopy over the three sites of the CeO_2(111) surface reproduces the trend shown in Fig. 1d. Measurements were done on the fourth ceria surface bilayer (see Fig. S1), in which an atomic arrangement close to the bulk ceria is expected.

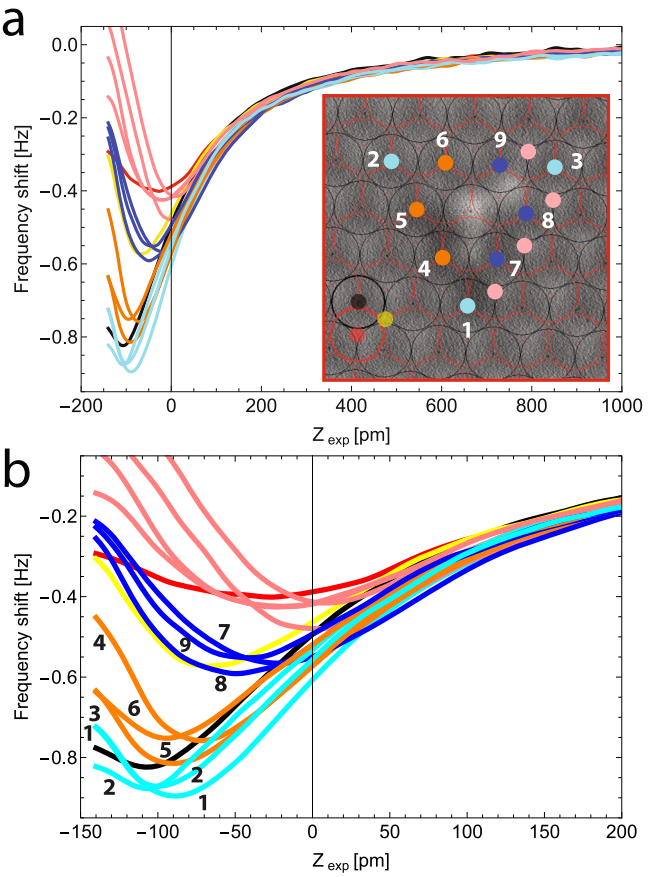

Fig. 7 | Spectroscopic curves measured at surface atomic sites surrounding a water molecule. a Sets of Δf curves measured over Ce and O positions around the water molecule, highlighted with a red square in Fig. 1a. The inset is a constant-height AFM image of the molecule, acquired before the spectroscopic measurement at a separation corresponding to the origin of the distance axis. Black and red lattices superimposed on the image highlight the cerium and oxygen surface positions, respectively. **b** Detail of the Δf curves close to the minima. Numbering and color link the corresponding curve to the acquisition location in inset image: curves over the Ce atoms are in cyan (1, 2, 3), orange (4, 5, 6) and blue (7, 8, and 9); and relevant curves over O atoms are displayed in pink color (see also Fig. S11). Curves measured over Ce (in black), O (in red), and CV (in yellow) sites far from the water molecule are included for comparison. Acquisition parameters were: A = 60 pm and f_0 = 994230 Hz.

DFT calculations

The adsorption and transition state structure optimizations, as well as the simulated force-distance calculations, were performed using DFT as implemented in the VASP code (version 5.4.4)[39–43] with the slab-supercell approach[61]. The projector augmented wave (PAW) method[62] was used to describe the valence electrons of the atomic species: Ce (4f, 5s, 5p, 5d, 6s), O (2s, 2p) and H (1s), with a plane-wave cutoff energy of 415 eV. The electron localization on Ce^{3+} atoms of the support has been treated by means of the DFT+U approach proposed by Dudarev et al.[63], with a U_{eff} value of $U - J$ = 4.5 eV for the Ce 4f electrons. We used the PBE exchange–correlation functional, the generalized gradient approximation (GGA) suggested by Perdew, Burke, and Ernzerhof (PBE)[44]. The vdW dispersion energy correction was considered by means of the so-called DFT-D3 approach[45,46].

Adsorption and transition state structure calculations

CeO_2(111) surfaces with (3 × 3) and (4 × 4) periodicities were modeled with an optimized lattice constant of 5.485 Å for bulk CeO_2. The (3 × 3) surface models have four O–Ce–O tri-layers, whereas the (4 × 4) models were built with only three tri-layers to save computational resources. Both models have sufficient separation between consecutive slabs (~ 12 and 27 Å, respectively). All atoms in the bottom O–Ce–O tri-layer were kept fixed at their optimized bulk-truncated positions during geometry optimization, whereas the rest of the atoms were allowed to fully relax. A (2 × 2 × 1) k-point mesh, according to the Monkhorst–Pack method[64], was used to sample the Brillouin zone for the (3 × 3) models, and only the Γ-point for the (4 × 4) surface. For the gas-phase calculations of the water molecule, a (15 × 15 × 15) $Å^3$ cell was employed, with Γ-point only.

Two Ce^{4+} are reduced to Ce^{3+} when an oxygen vacancy is generated. Following the previous work by Pan et al.[65] (which reported many different positions for the Ce^{3+} on a (4 × 4) surface at the HSE level[66,67]), we modeled the most stable configuration they found, where the Ce^{3+} are next-nearest neighbors of the vacancy (Fig. S7a and Fig. S8b). Note that this causes the two Ce^{3+} atoms to be neighbors (to each other) on the (3 × 3) model (Fig. S5). To check that our results on the stability of water and OH+H species were not significantly affected by this situation, and to ensure that the (3 × 3) results were reliable for the subsequent spectroscopic studies, we also calculated the crucial structures on the (4 × 4) model for the two most stable relative positions of the two Ce^{3+} atoms (Fig. S7b, c and Fig. S8c, d).

The adsorption energy of water was calculated as:

$$\Delta E_{ads} = E(H_2O/CeO_2(111)) - E(H_2O) - E(CeO_2(111)) \quad (1)$$

where $E(H_2O/CeO_2(111))$ is the energy of the structure with water adsorbed on the surface, $E(H_2O)$ is the energy of the molecule in the gas phase, and $E(CeO_2(111))$ is the total energy of the clean model surface.

To identify transition state structures, the climbing image nudged elastic band technique (CI-NEB) was used[68], and frequency calculations were employed to check that only one imaginary frequency was found for each of them. Activation energies (ΔE_{act}) are defined as the difference between the energy of the transition state (TS) and the initial state (IS).

Simulated frequency shift curves

The frequency shift curves were calculated from the forces obtained with a model probe that includes: i) a rigid CO molecule to describe the interaction of the sample with the oxygen-termination of the probe apex, which provides chemical sensitivity and ii) the mesoscopic part of the apex (the yellow cone in Fig. 1) whose only contribution is a long–range attraction. The interaction with the apex as a function of the probe height is calculated with DFT by vertically approaching the CO probe toward the surface, adding up the vertical component of the force over the two atoms of the CO molecule at each approach distance. The atoms of the water molecule and the first trilayer of the surface were allowed to relax at each step of the approach, while the remaining atoms in the surface were kept fixed. These relaxations are minimal for the calculation of force curves over sites of the bare ceria surface within the probe-surface distance range explored, and can safely be disregarded to speed up calculations, but play a crucial role in the description of the water response to the probe-sample interaction. The computed force curves were converted into frequency shift (Δf) curves using classical perturbation theory[34] and the efficient approach proposed by Giessibl[69].

To better compare calculated Δf curves and images with the experimental counterparts, we added the main contribution of the long–range interaction between probe and surface in the experiments to all the calculated Δf curves and images. To characterise the long–range interaction in the experiments, we fitted the experimental Δf curves over the long-range distance regime considering the analytical expression for the Δf originated by the van der Waals interaction force between a spherical probe and a plane,[32,70]:

$$F_{vdW}(z) = \frac{C}{(z)^2} \Rightarrow \Delta f_{vdW}(z) = \frac{f_0}{\sqrt{8\pi} \cdot k \cdot A^{3/2}} \cdot \frac{C}{(z)^{3/2}}, \quad (2)$$

where f_0, k, and A represent the free-oscillation resonant frequency, the effective stiffness, and the oscillation amplitude of the force sensor, respectively, z denotes the probe-surface separation, and C is a fitting parameter that accounts for the mesoscopic geometry of the probe.

For the calculation of the $\Delta f(z)$ curves from the atomic forces provided by DFT, we used the experimental values of f_0, and A (Fig. 1), and the value k was obtained from the specifications of the KolibriSensor[56]. The parameter C was determined by fitting the experimental $\Delta f(z)$ curves measured on the stoichiometric surface over the tail towards the free-oscillation regime, obtaining $C = -1.4311 \times 10^{-6}$ N pm^2 (Fig. S16). Using these parameters, we added the $\Delta f_{vdW}(z)$ background (cyan dotted line in Figs. 1d, S9 and S12) to each of the $\Delta f(z)$ curves and images obtained from the DFT-based atomic forces.

The calculated $\Delta f(z)$ curves provide a reference for the probe-surface distance in the experiments, which is measured as the relative displacement of the sample with respect to the probe (fixed in our experimental system). In our simulations, on the contrary, the probe-surface distance is well defined with an origin ($z = 0$) at the plane of the topmost oxygen layer of CeO_2 (111) surface. To estimate the probe-surface distance in the experiments, we shift the calculated $\Delta f(z)$ curves as a block (that is, preserving the relative distance between them as defined by the DFT calculations) until an acceptable alignment of the minima of all experimental and calculated curves is reached. This process yields the equivalence: $z_{exp} = 0 \Leftrightarrow z = 411$ pm.

Simulation of the constant-height AFM images

Constant-height AFM images were simulated using the FDBM[53,54,71] as implemented in the `DBSPM` GitHub repository: https://github.com/SPMTH/DBSPM. This method efficiently computes frequency shift images while preserving the accuracy of the DFT-calculated forces, enabling the high-fidelity reproduction of atomic resolution AFM images. FDBM calculates the total force between a probe with an inert termination, like a CO molecule, as the sum of three contributions: the short-range Pauli repulsion (SR), the electrostatic interaction (ES), and the van der Waals dispersion energy correction modeled by the D3-vdW method[45]. The SR and ES contributions were computed as:

$$V_{SR} = V_0 \int [\rho_{\text{probe}} \cdot \rho_{\text{surface}}]^{\alpha} \, dV, \quad (3)$$

$$V_{ES} = \int \rho_{\text{probe}} \cdot \Phi_{\text{surface}} \, dV, \quad (4)$$

where ρ_{probe} and ρ_{surface} represent the charge density of probe and surface, respectively, and Φ_{surface} is the electrostatic potential of the surface. These quantities are obtained from independent DFT calculations for the probe and sample. To obtain the short-range parameters (α, V_0), we fit the total force (SR + ES + $vdW_{DFT\text{-}D3}$) computed with the FDBM method to DFT force–distance curves calculated with a rigid CO probe positioned over representative sites of the reduced CeO_{2-x}(111) surface (Fig. S15). This process yields $\alpha = 1.08$ and $V_0 = 36.96$ eV/Å$^{3(2\alpha-1)}$, ensuring that FDBM reproduces the DFT forces accurately, in particular the short-range contribution involving oxygen atoms. Therefore, the model should accurately describe the interaction with water molecules adsorbed on the CeO_2(111) surface. Since the oxygen atom in the water molecule lies ~2 Å above the surface oxygens, images of water acquired at probe–surface distances ~5 Å should be well captured by the FDBM approach. The probe-surface long-range vdW force obtained from Eq. (2) is then added to obtain the total force used to generate the Δf images shown in Figs. 3, S10 and S11 (see Fig. S17 for a detailed description of the AFM image simulation workflow). The FDBM simulated images shown in Fig. 3 were performed for water adsorbed on the reduced CeO_{2-x}(111) surface.

Data availability

All DFT data supporting the findings of this study are available at Zenodo under the accession number https://zenodo.org/records/17360622. The repository includes the following files: `Structures.tar.gz`, containing the VASP files for all structures reported in the paper; `forces_and_freq_shifts.tar.gz`, containing the forces and frequency-shift data used to reproduce the figures of the manuscript; and `movies.tar.gz`, providing DFT spectroscopy animations in `.mp4` format. A detailed description of the structural data is provided in `Structures_README.txt`. The experimental data supporting the findings of this study are available from the author (O.C.) upon reasonable request.

Received: 22 August 2025; Accepted: 5 November 2025;
Published online: 23 January 2026

References

1. Trovarelli, A. Catalysis by ceria and related materials | Catalytic science series Vol. 2 (World Scientific Publishing Company, London, England, UK, 2002).
2. Montini, T., Melchionna, M., Monai, M. & Fornasiero, P. Fundamentals and catalytic applications of CeO_2-based materials. *Chem. Rev.* **116**, 5987–6041 (2016).

3. Dresselhaus, M. S. & Thomas, I. L. Alternative energy technologies. *Nature* **414**, 332–337 (2001).
4. Gorte, R. J. Ceria in catalysis: From automotive applications to the water–gas shift reaction. *AIChE J.* **56**, 1126–1135 (2010).
5. Deluga, G. A., Salge, J. R., Schmidt, L. D. & Verykios, X. E. Renewable hydrogen from ethanol by autothermal reforming. *Science* **303**, 993–997 (2004).
6. Park, S., Vohs, J. M. & Gorte, R. J. Direct oxidation of hydrocarbons in a solid-oxide fuel cell. *Nature* **404**, 265–267 (2000).
7. Xu, C. & Qu, X. Cerium oxide nanoparticle: a remarkably versatile rare earth nanomaterial for biological applications. *NPG Asia Mater.* **6**, e90 (2014).
8. Pulido-Reyes, G. et al. Untangling the biological effects of cerium oxide nanoparticles: the role of surface valence states. *Sci. Rep.* **5**, 15613 (2015).
9. Campbell, C. T. & Peden, C. H. Oxygen vacancies and catalysis on ceria surfaces. *Science* **309**, 713–714 (2005).
10. Wendt, S. et al. The role of interstitial sites in the Ti3*d* defect state in the band gap of titania. *Science* **320**, 1755–1759 (2008).
11. Rodriguez, J. A. et al. Activity of CeO_x and TiO_x nanoparticles grown on Au(111) in the water-gas shift reaction. *Science* **318**, 1757–1760 (2007).
12. Bhosale, R. R. et al. A decade of ceria based solar thermochemical H_2O/CO_2 splitting cycle. *Int. J. Hydrog. Energy* **44**, 34–60 (2019).
13. Stetsovych, O. et al. Atomic species identification at the (101) anatase surface by simultaneous scanning tunnelling and atomic force microscopy. *Nat. Commun.* **6**, 1–9 (2015).
14. Setvin, M. et al. Polarity compensation mechanisms on the perovskite surface $KTaO_3$(001). *Science* **359**, 572–575 (2018).
15. Wagner, M., Meyer, B., Setvin, M., Schmid, M. & Diebold, U. Direct assessment of the acidity of individual surface hydroxyls. *Nature* **592**, 722–725 (2021).
16. Wang, Z. et al. Surface chemistry on a polarizable surface: coupling of CO with $KTaO_3$(001). *Sci. Adv.* **8**, eabq1433 (2022).
17. Hütner, J. I. et al. Stoichiometric reconstruction of the Al_2O_3(0001) surface. *Science* **385**, 1241–1244 (2024).
18. Gross, L., Mohn, F., Moll, N., Liljeroth, P. & Meyer, G. The chemical structure of a molecule resolved by atomic force microscopy. *Science* **325**, 1110–1114 (2009).
19. Mönig, H. et al. Submolecular imaging by noncontact atomic force microscopy with an oxygen atom rigidly connected to a metallic probe. *ACS Nano* **10**, 1201–1209 (2016).
20. Wiesener, P. et al. Standardization of chemically selective atomic force microscopy for metal oxide surfaces. *ACS Nano* **18**, 21948–21956 (2024).
21. Shiotari, A. & Sugimoto, Y. Ultrahigh-resolution imaging of water networks by atomic force microscopy. *Nat. Commun.* **8**, 14313 (2017).
22. Peng, J. et al. Weakly perturbative imaging of interfacial water with submolecular resolution by atomic force microscopy. *Nat. Commun.* **9**, 122 (2018).
23. Tian, Y. et al. Visualizing eigen/zundel cations and their interconversion in monolayer water on metal surfaces. *Science* **377**, 315–319 (2022).
24. Wu, D. et al. Probing structural superlubricity of two-dimensional water transport with atomic resolution. *Science* **384**, 1254–1259 (2024).
25. Hong, J. et al. Imaging surface structure and premelting of ice Ih with atomic resolution. *Nature* **630**, 375–380 (2024).
26. Gritschneder, S., Namai, Y., Iwasawa, Y. & Reichling, M. Structural features of CeO_2(111) revealed by dynamic SFM. *Nanotechnology* **16**, S41 (2005).
27. Gritschneder, S., Iwasawa, Y. & Reichling, M. Strong adhesion of water to CeO_2(111). *Nanotechnology* **18**, 044025 (2006).
28. Grinter, D. C., Ithnin, R., Pang, C. L. & Thornton, G. Defect structure of ultrathin ceria films on Pt(111): Atomic views from scanning tunnelling microscopy. *J. Phys. Chem. C.* **114**, 17036–17041 (2010).
29. Fernández-Torre, D., Kośmider, K., Carrasco, J., Ganduglia-Pirovano, M. V. & Pérez, R. Insight into the adsorption of water on the clean CeO_2(111) surface with van der waals and hybrid density functionals. *J. Phys. Chem. C.* **116**, 13584–13593 (2012).
30. Röckert, A., Kullgren, J., Broqvist, P., Alwan, S. & Hermansson, K. The water/ceria(111) interface: computational overview and new structures. *J. Chem. Phys*. **152**, 104709 (2020).
31. Zhou, Q., Akber, H., Zhao, A., Yang, F. & Liu, Z. Interaction of water with ceria thin film. *ChemCatChem* **15**, e202300318 (2023).
32. Lantz, M. A. et al. Quantitative measurement of short-range chemical bonding forces. *Science* **291**, 2580–2583 (2001).
33. Sugimoto, Y. et al. Chemical identification of individual surface atoms by atomic force microscopy. *Nature* **446**, 64–67 (2007).
34. Giessibl, F. J. Forces and frequency shifts in atomic-resolution dynamic-force microscopy. *Phys. Rev. B* **56**, 16010–16015 (1997).
35. Torbrügge, S., Custance, O., Morita, S. & Reichling, M. Manipulation of individual water molecules on CeO_2(111). *J. Phys. Condens. Matter* **24**, 084010 (2012).
36. Mullins, D. R. et al. Water dissociation on CeO_2(100) and CeO_2(111) thin films. *J. Phys. Chem. C.* **116**, 19419–19428 (2012).
37. Torbrügge, S., Reichling, M., Ishiyama, A., Morita, S. & Custance, O. Evidence of subsurface oxygen vacancy ordering on reduced CeO_2(111). *Phys. Rev. Lett*. **99**, 056101 (2007).
38. Sugimoto, Y. et al. Atom inlays performed at room temperature using atomic force microscopy. *Nat. Mater.* **4**, 156–159 (2005).
39. Kresse, G. & Hafner, J. Ab initio molecular dynamics for liquid metals. *Phys. Rev. B* **47**, 558–561 (1993).
40. Kresse, G. & Hafner, J. Ab initio molecular-dynamics simulation of the liquid-metal–amorphous-semiconductor transition in germanium. *Phys. Rev. B* **49**, 14251–14269 (1994).
41. Kresse, G. & Furthmüller, J. Efficient iterative schemes for ab initio total-energy calculations using a plane-wave basis set. *Phys. Rev. B* **54**, 11169–11186 (1996).
42. Kresse, G. & Furthmüller, J. Efficiency of ab-initio total energy calculations for metals and semiconductors using a plane-wave basis set. *Comput. Mater. Sci.* **6**, 15–50 (1996).
43. Kresse, G. & Joubert, D. From ultrasoft pseudopotentials to the projector augmented-wave method. *Phys. Rev. B* **59**, 1758–1775 (1999).
44. Perdew, J. P., Burke, K. & Ernzerhof, M. Generalized gradient approximation made simple. *Phys. Rev. Lett.* **77**, 3865–3868 (1996).
45. Grimme, S., Antony, J., Ehrlich, S. & Krieg, H. A consistent and accurate ab initio parametrization of density functional dispersion correction (DFT-D) for the 94 elements H-Pu. *J. Chem. Phys.* **132**, 154104 (2010).
46. Grimme, S., Ehrlich, S. & Goerigk, L. Effect of the damping function in dispersion corrected density functional theory. *J. Comput. Chem.* **32**, 1456–1465 (2011).
47. Fronzi, M., Piccinin, S., Delley, B., Traversa, E. & Stampfl, C. Water adsorption on the stoichiometric and reduced CeO_2(111) surface: a first-principles investigation. *Phys. Chem. Chem. Phys.* **11**, 9188–9199 (2009).
48. Molinari, M., Parker, S. C., Sayle, D. C. & Islam, M. S. Water adsorption and its effect on the stability of low index stoichiometric and reduced surfaces of ceria. *J. Phys. Chem. C.* **116**, 7073–7082 (2012).
49. Kropp, T., Paier, J. & Sauer, J. Interactions of water with the (111) and (100) surfaces of ceria. *J. Phys. Chem. C.* **121**, 21571–21578 (2017).
50. Munir, S. et al. Strain effects on the adsorption of water on cerium dioxide surfaces and nanoparticles: a modeling outlook. *J. Phys. Chem. C.* **128**, 18451–18464 (2024).

51. Jerratsch, J.-F. et al. Electron localization in defective ceria films: a study with scanning-tunneling microscopy and density-functional theory. *Phys. Rev. Lett.* **106**, 246801 (2011).
52. Han, Z.-K., Duan, X., Li, X., Zhang, D. & Gao, Y. The dynamic interplay between water and oxygen vacancy at the near-surface of ceria. *J. Phys. Condens. Matter* **33**, 424001 (2021).
53. Ellner, M., Pou, P. & Pérez, R. Molecular identification, bond order discrimination, and apparent intermolecular features in atomic force microscopy studied with a charge density based method. *ACS Nano* **13**, 786–795 (2019).
54. Ventura-Macias, E., Romero-Muñiz, C., González-Sánchez, P., Pou, P. & Pérez, R. Are High Resolution Atomic Force Microscopy images proportional to the force gradient or the force maps? *Appl. Surf. Sci.* **634**, 157558 (2023).
55. Hapala, P. et al. Mechanism of high-resolution STM/AFM imaging with functionalized tips. *Phys. Rev. B* **90**, 085421 (2014).
56. Torbrügge, S., Schaff, O. & Rychen, J. Application of the kolibrisensor to combined atomic-resolution scanning tunneling microscopy and noncontact atomic-force microscopy imaging. *J. Vac. Sci. Technol. B* **28**, C4E12–C4E20 (2010).
57. Sugimoto, Y. & Onoda, J. Force spectroscopy using a quartz length-extension resonator. *Appl. Phys. Lett.* **115**, 173104 (2019).
58. Kim, K., Abe, M., Kawai, S. & Custance, O. Exploring partially reduced CeO_2(111) surface at the atomic scale using scanning probe microscopy. *Sci. Technol. Adv. Mater.* **26**, 2528596 (2025).
59. Albrecht, T. R., Grütter, P., Horne, D. & Rugar, D. Frequency modulation detection using high-*q* cantilevers for enhanced force microscope sensitivity. *J. Appl. Phys.* **69**, 668–673 (1991).
60. Šutara, F. et al. Epitaxial growth of continuous CeO_2(111) ultra-thin films on Cu(111). *Thin Solid Films* **516**, 6120–6124 (2008).
61. Payne, M. C., Teter, M. P., Allan, D. C., Arias, T. A. & Joannopoulos, J. D. Iterative minimization techniques for ab initio total-energy calculations: molecular dynamics and conjugate gradients. *Rev. Mod. Phys.* **64**, 1045–1097 (1992).
62. Blöchl, P. E. Projector augmented-wave method. *Phys. Rev. B* **50**, 17953–17979 (1994).
63. Dudarev, S. L., Botton, G. A., Savrasov, S. Y., Humphreys, C. J. & Sutton, A. P. Electron-energy-loss spectra and the structural stability of nickel oxide: an LSDA+U study. *Phys. Rev. B* **57**, 1505–1509 (1998).
64. Monkhorst, H. J. & Pack, J. D. Special points for Brillouin-zone integrations. *Phys. Rev. B* **13**, 5188–5192 (1976).
65. Pan, Y. et al. Titration of Ce^{3+} Ions in the CeO_2(111) Surface by Au adatoms. *Phys. Rev. Lett.* **111**, 206101 (2013).
66. Heyd, J., Scuseria, G. E. & Ernzerhof, M. Hybrid functionals based on a screened Coulomb potential. *J. Chem. Phys.* **118**, 8207–8215 (2003).
67. Krukau, A. V., Vydrov, O. A., Izmaylov, A. F. & Scuseria, G. E. Influence of the exchange screening parameter on the performance of screened hybrid functionals. *J. Chem. Phys.* **125**, 224106 (2006).
68. Henkelman, G., Uberuaga, B. P. & Jónsson, H. A climbing image nudged elastic band method for finding saddle points and minimum energy paths. *J. Chem. Phys.* **113**, 9901–9904 (2000).
69. Giessibl, F. J. A direct method to calculate tip–sample forces from frequency shifts in frequency-modulation atomic force microscopy. *Appl. Phys. Lett.* **78**, 123–125 (2001).
70. García, R. & Pérez, R. Dynamic atomic force microscopy methods. *Surf. Sci. Rep.* **47**, 197–301 (2002).
71. Zahl, P. et al. Hydrogen bonded trimesic acid networks on Cu(111) reveal how basic chemical properties are imprinted in HR-AFM images. *Nanoscale* **13**, 18473–18482 (2021).

Acknowledgements

This work was supported by NIMS grants (AG2030 and AM2100), by several Grant-in-Aid for Scientific Research (19H05789, 21H01812, 21K18876, 22H00285, 23KJ1516, 24K01350) from the Ministry of Education, Culture, Sports, Science and Technology of Japan (MEXT) and by the Spanish Ministry of Science, Innovation and Universities (MCIU), through projects PID2023–149150OB–I00 and PID2021-128915NB-I00, and the "María de Maeztu" Program for Units of Excellence in R&D (CEX2023–001316–M). E.F.V. acknowledges support from the Margarita Salas postdoctoral fellowship (Spanish MIU and European Union NextGenerationEU) and the MOMENTUM Program (MMT-24-ICP-01, Plan de Recuperación, Transformación y Resiliencia European Union NextGenerationEU). The Spanish Supercomputing Network (RES) is acknowledged for providing computational resources at the Marenostrum Supercomputer (BSC, Barcelona).

Author contributions

O.C., K.K., M.A., H.S.A. and S.K. performed the experiments and data analysis. M.G.L., E.F.V., P.P., M.V.G.P. and R.P. performed the DFT calculations and AFM simulations. O.C., M.G.L., E.F.V., P.P., M.V.G.P., and R.P. wrote the manuscript.

Competing interests

The authors declare no competing interests.

Additional information

Supplementary information The online version contains supplementary material available at https://doi.org/10.1038/s43246-025-01011-x.

Correspondence and requests for materials should be addressed to Oscar Custance or Ruben Perez.

Peer review information *Communications Materials* thanks Guangfu Liao and the other, anonymous, reviewer(s) for their contribution to the peer review of this work. A peer review file is available.